An Overview of Gravitational-Wave Sources

Chengchao Yuan

Department of Physics, Pennsylvania State University, University Park, 16802, PA, USA

(Dated: April 28, 2017)

Abstract

The direct detection of GW150914 heralds the beginning of gravitational-wave (GW) astronomy and from that day on, human beings acquired a new insight to explore the Universe. This article aims to provide a comprehensive overview of the physics of GWs, the detection techniques, the results from LIGO's first observing run and the applications to astrophysics. Starting from Einstein's general relativity, the author discussed the radiation and propagation of GWs under the weak-field approximation. The detectors, LIGO and its prototype resonant antennae are also introduced. Then, the author reviewed several potential GW candidates, including coalescing binaries, gravitational collapses, tidal disruption events and stochastic GW background. Relevant models and predictions are described.

I. INTRODUCTION

The history of astronomy is a history of receding horizons.
— Edwin P. Hubble

Physics is not a completed logical system and our understanding towards the nature has constantly been renewed by the development of theories and experimental techniques. Since the time of Galileo, astronomy relied on the observations of electromagnetic radiation. At present, as one of the most important tool in astronomy, multi-wavelength technique has broadened our eyesight from solar system to the galaxies billions of light years away from us. Nevertheless, we are still seeking for supplementary messengers beyond electromagnetic signals. In 1912, Victor Hess discovered the cosmic rays by sending an electrometer into the atmosphere along with a balloon[1]. The discovery of cosmic rays was widely regarded as the beginning of particle astrophysics, which provides a new way to study the internal structure of astronomical sources and the mechanism of high-energy processes. The story is totally changed in 2015, when the Advanced Laser Gravitational-Wave Observatory (LIGO) directly detected the signal of gravitational waves from the merger of a binary black holes. Predicted by general relativity, GWs provide a crucial link between general relativity and the frontier of astrophysics. The direct detection of GW150914[2] heralds the beginning of gravitational-wave (GW) astronomy and since then the era of multi-messenger astronomy, including electromagnetic signals, cosmic rays and gravitational waves, becomes practical.

Last several decades has witnessed a great leap in astronomy, due to the development of observing techniques. During this time, large ground-based telescopes and detector arrays were constructed; a batch of satellites that were dedicated to detect infrared, X-ray, gamma-ray signals were launched. Each progress has brought vitality and surprising discoveries into astronomy, the oldest science. With the detection of GW on September 14, 2015, a brand new window was opened. The physical nature of GW is completely different with electromagnetic wave. Because of its unique property, we can use GWs to sense some astronomical sources that optical telescopes cannot reach, such as the early universe when electromagnetic waves were not decoupled. Also, for those detected sources, GWs provide a totally new approach and some supplementary information may be obtained. Hence, it is meaningful to review the physical foundations, detections and predictions of GWs.

An overview of the general relativity is given in section I.1 followed by the GW fundamentals in section I.2 which covers the basic properties of GWs, such as plane-wave solutions, polarizations and energy flux. Section II concentrates on detecting techniques and results. The principle and designed of resonant antennas and laser interferometers are described in section II.1 and II.2 respectively. Section II.3 summarizes the GW events detected in LIGO's first observing run. Models and predictions of various astronomical sources are discussed in section III. These GW candidates are classified to coalescing binaries, gravitational collapses, tidal disruption events and stochastic GW backgrounds. Remarks are given in section IV.

A. General relativity and Einstein's equation

In this section, I want to introduce the basic physical and mathematical background of the general relativity and deduce the equation describing GWs.

According to Isaac Newton's *Principia*, the space is ideally rigid and time is absolute. The space is an arena where events take place and the objects cannot change the space.

Newtonian mechanics defined a set of inertial frames, in which the time is universal and the physical laws take the unique form. Because of the infinity of the modulus of space, gravitational waves cannot exist in this picture. One crucial step was taken in 1907 when Einstein proposed the principle of equivalence that at every point in an arbitrary gravitational field one can always find a locally inertial coordinate system (freely falling coordinate system) such that the laws of nature take the same form as in an inertial frame without the gravitational field[3]. Recalling the definition of differentiable manifold in which each point has a neighborhood that is homeomorphic to the Euclidean space , one can naturally link the gravitational field to differential geometry, or more precisely, Riemannian geometry with Riemannian metric $g_{\mu\nu}$.

From Principle of Equivalence, we can directly write down the equation of motion in the freely falling coordinate system $\{x^i\}$,

$$\frac{d^2x^i}{ds^2} = 0 \tag{1}$$

with $ds^2 = g_{\mu\nu}dx^\mu dx^\nu = c^2d\tau^2$ the proper interval. To find the equation of motion for arbitrary coordinate system $\{u^i\}$, we consider the transformation $x^i = x^i(\mathbf{u})$ and

$$0 = \frac{d^2x^i}{ds^2} = \frac{d}{ds}\left(\frac{\partial x^i}{\partial u^j}\frac{du^j}{ds}\right) = \frac{\partial x^i}{\partial u^j}\frac{d^2u^j}{ds^2} + \frac{\partial^2 x^i}{\partial u^i \partial u^j}\frac{du^i}{ds}\frac{du^j}{ds}. \tag{2}$$

Multiplying equation (2) by $\frac{\partial u^\lambda}{\partial x^i}$, we obtain the equation of motion

$$\frac{d^2u^\lambda}{ds^2} + \Gamma^\lambda_{\mu\nu}\frac{du^\mu}{ds}\frac{du^\nu}{ds} = 0 \tag{3}$$

where $\Gamma^\lambda_{\mu\nu}$, the affine connection, demonstrates the difference of differential operations between Euclidean geometry and Riemannian geometry. From this treatment we can see that the affine connection $\Gamma^\lambda_{\mu\nu}$ functions as the force in Newton's second law, which determines the dynamic behavior of particles in gravitational fields. On the other hand, as shown in equation (1), the Riemannian metric $g_{\mu\nu}$ determines the interval (proper time $d\tau^2 = ds^2/c^2$) between two events. In fact, the affine connection can be written as the derivatives of $g_{\mu\nu}$,

$$\Gamma^\lambda_{\mu\nu} = \frac{1}{2}g^{l\lambda}\left(\partial_\mu g_{\nu l} + \partial_\nu g_{\mu l} - \partial_l g_{\nu\mu}\right). \tag{4}$$

In general relativity, $g_{\mu\nu}$ plays the role of gravitational potential.

With these preparations, we are ready to construct the curvature tensor. Let's start from one peculiar property of curved space that the parallel displacements of a vector is path-dependent. The change of a vector ΔA_i after parallel displacement around an infinitesimal closed path is determined by the intrinsic property of the curved space. Integrating $\delta A_i = \Gamma^\lambda_{ij}A_\lambda dx^j$ along a contour and applying Stoke's theorem, we obtain $\Delta A_i = \oint_C \Gamma^\lambda_{ij}A_\lambda dx^j = \frac{1}{2}\int R^\lambda_{ijk}A_\lambda da^{jk}$, where da^{jk} is the infinitesimal area enclosed by the contour C and R^λ_{ijk}, named as the curvature tensor or Riemannian tensor, is defined through

$$R^\lambda_{ijk} = \frac{\partial\Gamma^\lambda_{ik}}{\partial x^j} - \frac{\partial\Gamma^\lambda_{ij}}{\partial x^k} + \Gamma^\lambda_{lj}\Gamma^l_{ik} - \Gamma^\lambda_{lk}\Gamma^l_{ij}. \tag{5}$$

By tensor contraction, we construct a second-rank tensor (the Ricci tensor) $R_{ik} = R^l_{ilk}$. It's worthy of pointing out that only the contraction of λ, j is physical, otherwise we get a null tensor. The reason is that $R_{\lambda ijk} = g_{\lambda\sigma}R^\sigma_{ijk}$ is antisymmetric about the indices $\{\lambda, i\}$ and $\{j, k\}$: $R_{\lambda ijk} = -R_{i\lambda jk}$, $R_{\lambda ijk} = -R_{\lambda ikj}$. In flat space where no gravitational field exists, the Riemannian metric reduces to Minkowski metric $\eta^{\mu\nu}$ with the diagonal elements $(1, -1, -1, -1)$ and the curvature tensor is a null tensor. Finally, by contracting R_{ik}, we obtain a scalar $R = g_{ik}R^{ik}$ which is invariant under coordinate transformation and reflects the curvature of spacetime. So far, we have gathered all ingredients for the geometrical part of the field equation

$$R^{\mu\nu} - \frac{1}{2}g^{\mu\nu}R = \frac{8\pi G}{c^4}T^{\mu\nu}. \tag{6}$$

The left hand side describes the momentum and energy of matter and the equation represents a profound and innovative hypothesis that the curvature of spacetime is determined by the energy-momentum tensor $T^{\mu\nu}$. According to the equation field, the coupling constant of gravitational interaction is $G_F = G/c^4 \approx 10^{-44}$ N^{-1} corresponding to the elastic modulus of space in the order of 10^{30} Pa. Only catastrophic astronomical event can produce detectable spacetime ripples; examples including coalescing binaries (black hole - black hole, black hole - neutron star, etc), gravitational collapses (gamma-ray bursts and core-collapse supernovae), tidal disruption events and the inflationary universe.

As for electromagnetic fields, the conservation of energy and momentum is given by $\partial_k T^{ik} = 0$. However, with the presence of gravitational field, $D_\nu T^{\mu\nu} = 0$ does not represent any conservation law. Here D_ν is the covariant derivative operator and is defined by $D_\nu T^{\mu\nu} = \partial_\nu T^{\mu\nu} + \Gamma^\nu_{k\nu}T^{\mu k}$, the second term demonstrates the change of a vector due to the curvature of space when performing parallel displacement while the ordinary derivative $\partial_\nu T^{\mu\nu}$ corresponds to the infinitesimal change of a vector itself. In general relativity, the overall energy and momentum of matter and gravitational field is conserved through

$$\partial_\nu[-g(T^{\mu\nu} + t^{\mu\nu})] = 0, \tag{7}$$

where $g =$det$(g^{\mu\nu})$ is the determinant of Riemannian metric and $t^{\mu\nu}$, the energy-momentum tensor of gravitational field, is determined by[4]

$$(-g)(T^{\mu\nu} + t^{\mu\nu}) = \frac{c^4}{16\pi G}\partial_l\partial_m\left[(-g)(g^{\mu\nu}g^{lm} - g^{\mu l}g^{\nu m})\right]. \tag{8}$$

Recalling the physical meaning of $t^{\mu\nu}$, we can naturally write down the energy density and energy flow of gravitational radiation as t^{00} and $ct^{0\alpha}$ ($\alpha = 1, 2, 3$ correspond to the flow along x, y, z axes) respectively. In section 1.B, we will use a simplified $t^{\mu\nu}$ to study the energy loss rate due to GW raidation.

B. Foundations of gravitational waves

Considering the symmetry of $g^{\mu\nu}$, the field equation can be reduced into 10 nonlinear equations. Unfortunately, it is extremely hard or even impossible to find rigorous solutions in general situation. There are two approached to alleviate this problem. One is to linearize these equations by introducing weak-field perturbation to Minkowski metric, $g^{\mu\nu} = \eta^{\mu\nu} + h^{\mu\nu}$, where $|h^{\mu\nu}| \ll 1$. Another method is to find the exact solutions un-

der some special assumptions or constraints, one famous example of exact solutions is the Friedmann-Lematre-Robertson-Walker metric which describes the isotropic, homogeneous universe. This section focuses on the first approach to derive the equations of gravitational radiation. The validity of weak-field approximation is ensured when the intensity of observed gravitational wave satisfies $|h^{\mu\nu}| \ll 1$. In most cases, fortunately, it is true.

1. Weak-field approximation, plane waves

It is convenient to rewrite the field equation into covariant form. By introducing a perturbation $h_{\mu\nu}$ to $\eta_{\mu\nu}$, the metric tensor is $g_{\mu\nu} = \eta_{\mu\nu} + h_{\mu\nu}$. To the first order of h, the affine connection can be written as

$$\Gamma^{\lambda}_{\mu\nu} = \frac{1}{2}\eta^{\lambda\rho}(\partial_\mu h_{\rho\nu} + \partial_\nu h_{\rho\mu} - \partial_\rho h_{\mu\nu}). \tag{9}$$

The curvature tensor is then

$$R_{\mu\nu} = \partial_\nu \Gamma^{\lambda}_{\lambda\mu} - \partial_\lambda \Gamma^{\lambda}_{\mu\nu} + O(h^2). \tag{10}$$

As already mentioned that $g_{\mu\nu}$ functions as the gravitational potential, the solution of field equation cannot be unique unless one gauge is fixed. Without violating the weak-field condition, we can consider the coordinate transformation $\bar{x}^\mu = x^\mu + \epsilon^\mu(\mathbf{x})$, if $\partial_\nu \epsilon^\nu$ is of the same order of $h_{\mu\nu}$, we can assert $\bar{h}_{\mu\nu} = h_{\mu\nu} - \partial_\nu \epsilon_\mu - \partial_\mu \epsilon_\nu$ is also a solution to the field equation which describes the same gravitational field. To simplify the equations, we choose a particular proviso $g^{\mu\nu}\Gamma^{\lambda}_{\mu\nu} = 0$ which determines the so called harmonic coordinate system. Substituting $\Gamma^{\lambda}_{\mu\nu}$ and $R_{\mu\nu}$ into the field equation, we obtain the equation of $h_{\mu\nu}$ to the first order

$$\begin{aligned} \partial_\rho \partial^\rho h_{\mu\nu} &= \frac{-16\pi G}{c^4} S_{\mu\nu}, \\ S_{\mu\nu} &= T_{\mu\nu} - \frac{1}{2}\eta_{\mu\nu} T^{\lambda}_{\lambda}. \end{aligned} \tag{11}$$

In the source part $S_{\mu\nu}$, because $t_{\mu\nu}$ is of the second order of h, we only consider $T_{\mu\nu}$ to the lowest order of h.

Now we investigate plane-wave solutions to equation (7) when the GWs are propagating in vacuum. In this case, the far-field approximation is valid and therefore we take the energy-momentum tensor $T_{\mu\nu}$ to be zero. Analogous to electromagnetic waves, the general solution of $\partial_\rho \partial^\rho h_{\mu\nu} = (\frac{1}{c^2}\frac{\partial^2}{\partial t^2} - \nabla^2) h_{\mu\nu} = 0$ is

$$h_{\mu\nu} = e_{\mu\nu} \exp(i k_\lambda x^\lambda) + \text{c.c.} \tag{12}$$

Here, $e_{\mu\nu}$ indicates how $h_{\mu\nu}$ is polarized and is thereby called polarization tensor. It is trivial that all elements of $h_{\mu\nu}$ should be real, so the complex conjugate is also included in the solution and to satisfy the wave equation we require $k_\mu k^\mu = 0$. Under weak-field approximation, the gauge of harmonic coordinate system reduces to $\partial_\mu(\eta^{\mu\rho} h_{\rho\nu}) = \frac{1}{2}\partial_\nu(\eta^{\sigma\rho} h_{\sigma\rho})$ which leads

to the confinement to the polarization tensor

$$k_\mu \eta^{\mu\lambda} e_{\lambda\nu} = \frac{1}{2} k_\nu \eta^{ij} e_{ij}. \tag{13}$$

In general, there should be ten independent elements in $e_{\mu\nu}$ since it is symmetric. Applying four the constraints from equation (13), the number is lowered to six. For a generic gravitational wave, only two components of $e_{\mu\nu}$ are physically significant. We can see this by considering a wave traveling in $+z$ direction and a coordinate transformation $\bar{x}_\mu = x_\mu + \epsilon_\mu(\mathbf{x})$. The new polarization is $\bar{e}_{\mu\nu} = e_{\mu\nu} + k_\mu \epsilon_\nu + k_\nu \epsilon_\mu$. Noting that $k^\mu = (\omega/c, 0, 0, k)$, only e_{11} and e_{12} are invariant under the transformation while the others dependent on the magnitude of $\boldsymbol{k}$. In other words, for a plane wave, we can always find a new coordinate system in which only $e_{11} = -e_{22}$ and $e_{12} = e_{21}$ are nonzero. Hence, $h_{\mu\nu}$ can be decomposed into the superposition of *plus* mode h_+ and *cross* mode $h_\times$

$$h_{\mu\nu} = \left[h_+ e^+_{\mu\nu} + h_\times e^\times_{\mu\nu} \right] \cos(k_\lambda x^\lambda). \tag{14}$$

In matrix form, $e^+_{\mu\nu}$ and $e^\times_{\mu\nu}$ are respectively

$$\epsilon^+_{\mu\nu} = \begin{bmatrix} 0 & 0 & 0 & 0 \\ 0 & 1 & 0 & 0 \\ 0 & 0 & -1 & 0 \\ 0 & 0 & 0 & 0 \end{bmatrix}, \ \epsilon^\times_{\mu\nu} = \begin{bmatrix} 0 & 0 & 0 & 0 \\ 0 & 0 & 1 & 0 \\ 0 & 1 & 0 & 0 \\ 0 & 0 & 0 & 0 \end{bmatrix} \tag{15}$$

To fully understand the physical meaning of $e^{+,\ \times}_{\mu\nu}$, we show that the force field in the post-Newtonian limit. From the geodesic equation (3), we obtain the effective gravitational acceleration[5]

$$\begin{aligned} a_x &= \frac{1}{2} \left(\ddot{h}_+ e_{11} \hat{x} + \ddot{h}_\times e_{12} \hat{y} \right) \cdot \boldsymbol{r}; \\ a_y &= \frac{1}{2} \left(-\ddot{h}_+ e_{11} \hat{y} + \ddot{h}_\times e_{12} \hat{x} \right) \cdot \boldsymbol{r}; \\ a_z &= 0. \end{aligned} \tag{16}$$

For + polarization ($e_{12} = 0$) and $\times$ polarization ($e_{11} = 0$), the schematic line-of-force diagrams at $k_\lambda k^\lambda = 0$ are illustrated in figure 1. These diagrams depict the compressing and stretching directions of $h_{+,\ \times}$. The + polarization relates to the oscillation of spacetime along the x, y axes while $\times$ polarization along the bisectors of the first and third quadrants. The polarization property of GWs also asserts special requirements to the configuration of detectors. Details pertaining to the GW detectors are included in section II.

2. Energy and momentum of GWs

To determine the energy flow of GWs along z direction, we need to find $t^{\mu\nu}$ to the lowest order of h. Because $g_{\mu\nu} = \eta_{\mu\nu} + h_{\mu\nu}$ satisfies the first-order field equation, $R^{(1)}_{\mu\nu}$, the Ricci tensor to the first order of h, vanishes. Therefore, to obtain the non-vanishing $t_{\mu\nu}$, we have

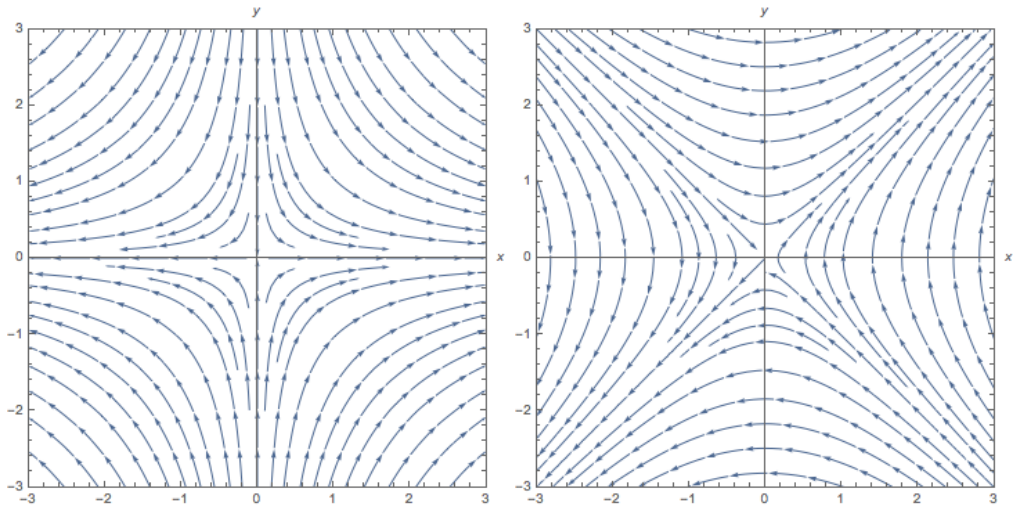

FIG. 1. The line-of-force diagrams for + polarization (left) and × (right) at phase 0

to write it as a function of $R^{(2)}_{\mu\nu} \sim O(h^2)$,

$$t_{\mu\nu} \approx \frac{c^2}{8\pi G}\left[R^{(2)}_{\mu\nu} - \frac{1}{2}\eta_{\mu\nu}\eta^{ij}R^{(2)}_{ij}\right]. \tag{17}$$

Instead of the instantaneous quantity, we are more interested in the average energy flow over one period. More importantly, $t_{\mu\nu}$ is not gauge-invariant and this problem can be circumvented by averaging over several periods. Combining equation (13) and equation (17), the energy-momentum tensor of a GW traveling in z direction is

$$< t_{\mu\nu} >= \frac{c^4 k_\mu k_\nu}{16\pi G}\left(|h_+|^2 + |h_\times|^2\right). \tag{18}$$

Since $k_x = k_y = 0$, the direction of energy flow is the same with the direction of $\boldsymbol{k}$. Because the wave vector satisfies $k_\mu k^\mu$=0, we except $k^0 k^3 = (\omega/c)k = w^2/c^2$ and $\omega^2|h_{\mu\nu}|^2 = |\dot{h}_{\mu\nu}|^2$. The energy-flow in z direction can be written as

$$S_z = ct^{03} = \frac{c^3}{16\pi G}\left[|\dot{h}_{11}|^2 + |\dot{h}_{12}|^2\right]. \tag{19}$$

In the rest part of this section, we focus on the radiative mechanisms of GWs when weak-field approximation ($|h| \ll 1$) and far-field condition ($r \gg R_0$ and $\lambda \gg R_0$, where R_0 characterize the dimension of sources and λ is the wavelength of GW) are simultaneously satisfied. Under these assumptions, the leading term of the multipole expansion is the quadrupole component. Inside the source region, we can directly write down the general solution of the equation of retard potential (eqn. 11)

$$h^{\mu\nu} = \frac{4G}{c^4 R}\int d^3\boldsymbol{r}' S^{\mu\nu}\left(r', \frac{t - |\boldsymbol{R} - \boldsymbol{r}'|}{c}\right). \tag{20}$$

Now, we confront the integral in equation (20). Using the gauge introduced in section I.B.1

and some mathematical techniques, equation (20) yields

$$S_z = \frac{G}{36\pi c^5 R^2}\left[\left(\frac{\dddot{D}_{11} - \dddot{D}_{22}}{2}\right)^2 + \dddot{D}_{12}^2\right], \tag{21}$$

where $D_{ij} = \int \rho(3x_i x_j - r^2\delta_{ij})dV$ is the mass quadrupole moment.

Obviously, the two terms in equations (21) represent energy flow contributed by two independent polarizations. It is useful to generalize the result so that the result does not depend on the direction of $\boldsymbol{k}$ (in the previous derivation, we assumed $\boldsymbol{k} = k\hat{z}$). To achieve this goal, we utilize the basic property of tensors that the scalars are invariant under coordinate transformations. Hence $\dddot{D}_{ij}e^{ij} = \dddot{D}'_{ij}e^{ij\prime}$, where e^{ij} is the polarized tensor. Moreover, multiplying the energy flow by $R^2 d\Omega$, we obtain the invariant radiative intensity per unit solid angle[4]

$$dI = \frac{G}{72\pi c^5}(\dddot{D}_{ij}e^{ij})^2 d\Omega. \tag{22}$$

Thus far, we have derived most of the equations for computing the distortion of spacetime due to GWs. Despite these results are obtained from the weak-field and far-field approximations, they agree very well with observations. For example, the strain amplitudes detected by LIGO are in the order of 10^{-22} which shows the precondition $h \ll 1$ is perfectly met. In addition, the first directly detected GW signal was generated about hundreds Mpc away, greatly larger than the wavelength. In section III, we will apply these equations to various astronomical GW candidates, including coalescing binary systems, gravitational collapses and tidal disruption events.

II. GRAVITATIONAL-WAVE DETECTORS

Observations are meaningless without a theory to interpret them.
—Raymond A. Lyttleton

As one crucial part in general relativity, GWs have constantly attracted scientists to propose and modify the detecting methods and facilities. Experiments that dedicated to the detection of GWs dates back to the middle of last century. The biggest obstacle of relevant experiments is tenuity of gravitational strains. The perturbation $h_{\mu\nu}$ in Riemanian tensor lead to a deformation of objects $\Delta L \sim L \times h$. As for astronomical sources, the typical upper bound of h is around $h \sim 10^{-21}$ and thus ΔL can be easily estimated to be 10^{-18} m if the size of the detector is 1 km. This displacement is roughly seven orders of magnitude smaller than Bohr radius $a = 5.26 \times 10^{-11}$ m which characterizes the dimension of atoms. How to improve the sensitivity of detectors so that the small change of distance can be precisely measured has become the prior consideration when designing a GW antenna. Here, we focus on two scenarios that start from two different points. The first relies on the microscopic structure of crystals while the other attempts to use a modified Michelson interferometer. These two kinds detectors are called resonant quadrupole antenna and laser interferometer detectors respectively.

In 1960, J. Weber[6][7] proposed that we can make use of a crystal as resonant quadrupole antenna to detect the displacements of mass points produced by GWs. The strains in one crystal can lead to electric polarization and h can be determined from the induced electric potential difference. After that, a series of experiments has been conducted and J. Weber managed to observe several probable events[8] in 1968 using two detectors separated about 2 km. Another approach, using laser interferometers to investigate the relative displacement of mirrors, was firstly published by M. Gertsenshtein and V. Pustovoit. Since then, J. Weber, R. Weiss et al realized this scenario by identifying noise sources, optimizing designs and adding amplification systems. With these efforts, the ideas and prototypes have eventually become practical. Details pertaining to principles of laser interferometer detectors and configurations of LIGO and VIRGO are described in section III B.

A. Resonant quadrupole antennas

In this section, we study how GWs with polarization $e_{\mu\nu}$ and wave vector k^μ interact with quadrupole antennas. Following the procedure in quantum scattering, the perturbed Riemannian tensor $h_{\mu\nu}$ at large distance can be decomposed into a plane wave and an outgoing scattered spherical wave,

$$h_{\mu\nu}(\boldsymbol{r}, t) = \left[e_{\mu\nu} e^{\boldsymbol{k}\cdot\boldsymbol{r}} + f_{\mu\nu}(\hat{r}) \frac{e^{i\boldsymbol{k}\cdot r}}{r} \right] e^{-i\omega t} \tag{23}$$

where $f_{\mu\nu(\hat{r})}$ is the scattering amplitude. Once $f_{\mu\nu}$ is determined, we can furthure conclude the polarization-dependent differential cross section $d\sigma_{\mu\nu}/d\Omega = |f_{\mu\nu}|^2$ and total cross section $\sigma_{tot} = 4\pi/k \ \mathrm{Im}(f_{\mu\nu})$ using optical theorem. For full scattering amplitude we expand $f_{\mu\nu}$ as

a series of phase shifts $\delta^l_{\mu\nu}(\theta)$,

$$f_{\mu\nu} = \frac{1}{k}\sum_l (2l+1)e^{i\delta^l_{\mu\nu}} \sin\delta^l_{\mu\nu} P_l(\cos\theta), \tag{24}$$

where $P_l(\cos\theta)$ is Legendre polynomial. The phase shift of each polarization component can be evaluated from the boundary conditions at the edge of scatterer. As for a given antenna with resonant frequency ω_0 and full width at half maximum Γ, the frequency-dependent scattering amplitude is given by the $e^{-i\omega_0}$ component of Fourier series. Here, we follow the approach in [3][6] by introducing a parameter η that characterizes the fraction of energy dissipated in outgoing GWs when the incident GW interacts with the antenna. The total cross section is now

$$\sigma_{tot} = \frac{10\pi\eta c^2}{\omega^2}\frac{\Gamma^2/4}{(\omega-\omega_0)^2+\Gamma^2/4}. \tag{25}$$

In experiment, the antenna should be tuned so that the frequency of incident GW should to fall within the effective bandwidth of the antenna. When one bunch of GWs sweeps the antenna, a small amount of energy is absorbed by the antenna. Oscillator inside the antenna will transit to excited states. If the change of energy can be extracted from noses, we can reconstruct the energy flow $ct^{0\alpha}$. Given the energy flux $\Phi(\omega)$ of incident GW, the power absorbed by a resonant antenna is

$$P = \int \sigma_{tot}(\omega)\Phi(\omega)d\omega \approx \frac{1}{2}\pi\eta\lambda^2\Phi(\omega_0)\Gamma \tag{26}$$

where $\lambda = 2\pi c/\omega$ is the wavelength. According to J. Weber's paper, a crystal with constants similar to polarized barium titanate on which sinusoidal gravitational waves are incident the absorbed power is, roughly,

$$P \approx 10^{-19}\left(\frac{\Phi(\omega_0)}{\text{erg cm}^{-2}\text{ s}^{-1}}\right)\text{erg s}^{-1} \tag{27}$$

To improve the sensitivity, the cross correlator receives signals from two conducting boxes in which crystals and amplifiers are deployed, as illustrated in figure 2. The benefit of this arrangement is that only GW can cause correlated outputs while random thermal noses are filtered in cross correlator[9]. Employing these features, the author predicted that GWs with $\Phi(\omega_0) \geq 10^{-4}$erg cm^{-2} s^{-1} should be detectable.

In 1968, three GW events were detected from February to March using two separated detectors with extremely low probability of false alerts. However, to precisely conclude the waveform and GW sources, larger separation and broadened frequency window are required for future experiments.

B. The Laser Interferometer Gravitational-Wave Observatory (LIGO)

Currently, the primary contributions to detect GWs employ the technique of laser interferometry to record the changes of the lengths between different optical paths. The anisotropy and polarization of GWs can be sensed by the discrepancies of ΔL between floating mirrors deployed in optical arms of varying orientations. To understand the technique

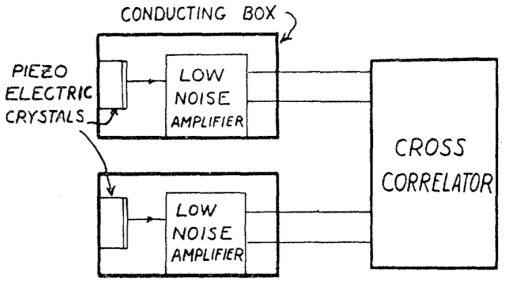

FIG. 2. Schematic diagram of correlated resonant antennas.

of laser interferometry, we can start from the principle of simple Michelson interferometer. In a Michelson interferometer, a light beam is splitted into two arms by a beamspliter. In each optical arm, the light is reflected back to the beamspliter by a mirror. When two light beams encounter at the beamspliter, they combine to a single beam interferometrically

$$I = I_0[1 + \cos(\delta)] \tag{28}$$

where I_0 and I are intensities of incident and output light beams. The phase difference of two optical paths δ is determined by the wavelength of the light λ and the effective aberration of light ΔL_{eff},

$$\delta = \frac{\Delta L_{eff}}{\lambda} = \frac{hL_{eff}}{\lambda}. \tag{29}$$

From this equation, we conclude that to produce obvious interference effect we need to increase the effective aberration of light and lower the wavelength without eliminating coherence. That is why the GW detectors use high-power laser to sense the ΔL and use oscillating cavity to prolong ΔL_{eff} so that the splitted light beam will travel N rounds in one arm before combing at the beamspliter. Then $\Delta L_{eff} = N \times hL$, which means the strain is amplified N times.

The LIGO system consists two detectors[10] at Hanford, WA (H1 detector) and Livingston, LA (L1 detector), as illustrated in Figure 3(a). Each site operates one LIGO detector and we can deduce the propagating direction of gravitational waves from the time differences between these two detectors. Each detector is a modified Michelson interferometer. When one gravitational wave sweeps the Earth, the spatial length in different directions will be either stretched or compressed. The measured difference in x direction (L_x) and y direction (L_y) will give the gravitational-wave strain amplitude (h) projected into the director through the relation $L_x - L_y = h_{xy}(t)L$, where L=4km is the original length of each arm. The differential length will cause a phase difference between two laser beams and hence the gravitational-wave strain is converted to optical signal in the photodetector.

One of the biggest challenges is to achieve sufficient sensitivity to measure $h(t)$ to the order of 10^{-22}. The system employs three major modifications[11] to the Michelson interferometer. Firstly, the laser beam in each arm can oscillate between two test masses for 300 rounds. Therefore, the differential length is accumulated and amplified by a factor of 300. Secondly, in each arm the laser is boosted from 20 W to 100 kW, which maintains a good coherence between two beams and therefore improves the resolution. Thirdly, one signal cycling system is added to the output terminal. This system can optimize the signal extraction by extending

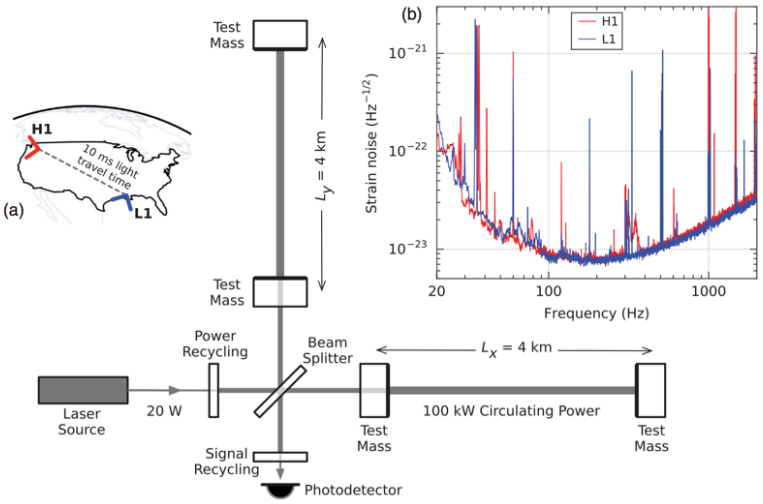

FIG. 3. (a) the schematic diagram of LIGO detectors [2] and the instrument noise for each detector as a function of frequency of incoming gravitational waves.

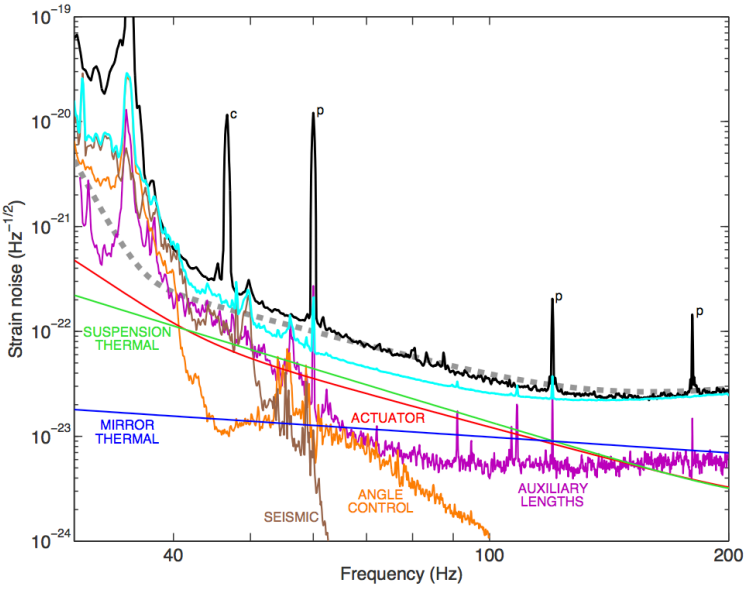

FIG. 4. The known contributors to H1 detector. The black line is the measured noise while dashed-gray line is the ideal noise from equation (30). The components are labelled and colored.

the bandwidth of each arm cavity. With these modifications, the system noise is controlled under 10^{-22}[12] and the sensitivity even reaches 10^{-23} at 200 Hz (see Fig 1b). The spikes in this figure are caused by the vibration modes of each part of the system. By design, the major noise source above 100 Hz is shot noise which is dominated by Poisson processes of photon detection. For laser interferometers, the ideal shot-noise of the strain is:

$$\delta h(f) = \sqrt{\frac{\pi\hbar\lambda}{\eta P_{BS} c}} \frac{\sqrt{1+(4\pi f\tau_s)^2}}{4\pi\tau_s} \tag{30}$$

Category	Description
Transient-modeled waveforms	The coalescing binary search. For these sources, precise and stable results can be obtained.
Transient-unmodeled waveforms	The GW burst search. Transient systems like GRB, TDEs that can produce GW bursts that can only be imperfectly modeled due to the random mechanisms of these events.
Continuous, narrow-band waveforms	The continuous wave sources search. An example is the GW from braking/accreting neutron stars.
Continuous, broad-band waveforms	The stochastic GW background search. Processes in early universe may produce such GWs.

TABLE I. Descriptions of LIGO GW search categories

where λ is laser wavelength, τ_s is the storage time in each arm cavity, f is GW frequency, P_{BS} is the power absorbed by the beamspliter and η is the quantum efficiency which represent the ratio of output SNR (signal-to-noise ratio) and input SNR. Assuming $\eta = 0.9$ and $P_{BS} =$ 250W, we expect the shot noise to be $10^{-23}/\sqrt{\text{Hz}}$. Experimentally, the noise can be estimated using stimulus-response tests. One known wave is fed to the system and the noise can be estimated from the corresponding response. The estimated and measured noises are shown in figure 4. The colored lines represent different components including seismic and thermal noise, auxiliary degree-of-freedom noise, actuation noise. Detailed discussions pertaining the relevant contributors can be found in [13]. LIGO is designed to differentiate GW waveforms from various sources. According to the continuity, the signals can be classified into categories of transient and continuous waveforms. Each category is further divided into two subgroups by analysis techniques. Astronomical sources of these categories are summarized in table 1. Predictions and results of relevant sources are discussed in section IV.

C. LIGO's first observing run

In this section we report three GW events in LIGO's first observing run from September 12, 2015 to January 19, 2016. The detectors achieved unprecedented sensitivity to GWs in the frequency range from tenths of Hz to thousands of Hz, which enables us to record the GW signals from evolutionary stages of binary black holes (BBH). During this observing period, based on the transient-modeled search, two signals, GW150914[2] and GW151226[14], were identified to be GW signals with a significance greater than 5σ. In addition, one possible GW event, LVT151012[15], with a lower significance was also detected. Waveforms of these three events as well as the noise curve of LIGO are shown in figure 5[15]. As we can observe in the right panel of figure 5, the time evolution of these signals show a chirp feature that initially the frequency increase monotonically with amplitude before dumping. This corresponds to the spiral phase of BBH and the amplitude reaches maximum at merger. After that, GW dumps rapidly to zero as the new-born black hole rings down to a stable state. Statistically,

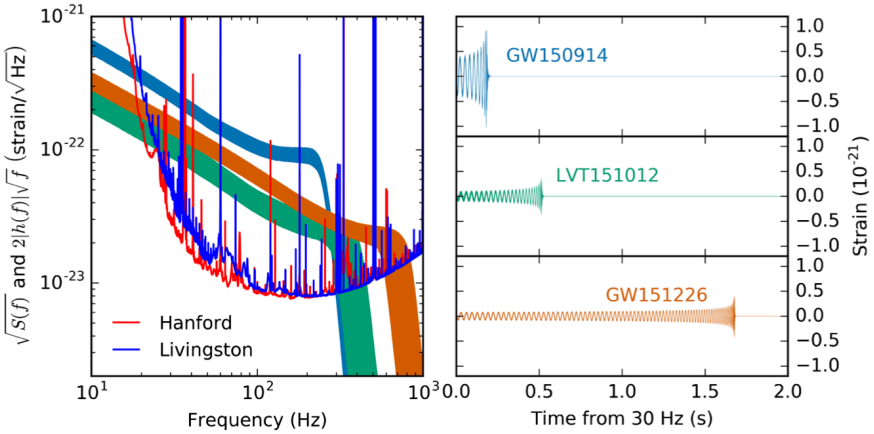

FIG. 5. Left: the measured noise curve and recovered strains of GW150914, GW151226 and LVT151012 in the effective detection window. Right: Evolution of GW signals at 30 Hz.

Event	GW150914	GW151226	LVT151012
Signal-to-noise ratio ρ	23.7	13.0	9.7
False alarm rate FAR/yr^{-1}	$< 6.0 \times 10^{-7}$	$< 6.0 \times 10^{-7}$	0.37
p-value	7.5×10^{-8}	7.5×10^{-8}	0.045
Significance	$> 5.3\sigma$	$> 5.3\sigma$	1.7σ
Primary mass $m_1^{\rm source}/\mathrm{M}_\odot$	$36.2^{+5.2}_{-3.8}$	$14.2^{+8.3}_{-3.7}$	23^{+18}_{-6}
Secondary mass $m_2^{\rm source}/\mathrm{M}_\odot$	$29.1^{+3.7}_{-4.4}$	$7.5^{+2.3}_{-2.3}$	13^{+4}_{-5}
Chirp mass $\mathcal{M}^{\rm source}/\mathrm{M}_\odot$	$28.1^{+1.8}_{-1.5}$	$8.9^{+0.3}_{-0.3}$	$15.1^{+1.4}_{-1.1}$
Total mass $M^{\rm source}/\mathrm{M}_\odot$	$65.3^{+4.1}_{-3.4}$	$21.8^{+5.9}_{-1.7}$	37^{+13}_{-4}
Effective inspiral spin $\chi_{\rm eff}$	$-0.06^{+0.14}_{-0.14}$	$0.21^{+0.20}_{-0.10}$	$0.0^{+0.3}_{-0.2}$
Final mass $M_{\rm f}^{\rm source}/\mathrm{M}_\odot$	$62.3^{+3.7}_{-3.1}$	$20.8^{+6.1}_{-1.7}$	35^{+14}_{-4}
Final spin $a_{\rm f}$	$0.68^{+0.05}_{-0.06}$	$0.74^{+0.06}_{-0.06}$	$0.66^{+0.09}_{-0.10}$
Radiated energy $E_{\rm rad}/(\mathrm{M}_\odot c^2)$	$3.0^{+0.5}_{-0.4}$	$1.0^{+0.1}_{-0.2}$	$1.5^{+0.3}_{-0.4}$
Peak luminosity $\ell_{\rm peak}/(\mathrm{erg\,s}^{-1})$	$3.6^{+0.5}_{-0.4} \times 10^{56}$	$3.3^{+0.8}_{-1.6} \times 10^{56}$	$3.1^{+0.8}_{-1.8} \times 10^{56}$
Luminosity distance $D_{\rm L}/\mathrm{Mpc}$	420^{+150}_{-180}	440^{+180}_{-190}	1000^{+500}_{-500}
Source redshift z	$0.09^{+0.03}_{-0.04}$	$0.09^{+0.03}_{-0.04}$	$0.20^{+0.09}_{-0.09}$
Sky localization $\Delta\Omega/\mathrm{deg}^2$	230	850	1600

FIG. 6. Important parameters of three events.

we can estimate the SNR of each event by integrating the signal in the detection window. We can roughly think that the SNR is proportional to the area between the noise curve and the signal curve, as shown in figure 5.

Since the waveforms agree well with the expected BBH evolutions, we can use existing models to fit basic physical parameters of the binary system. For example, the chirp mass $M = (m_1 m_2)^{3/5}/(m_1 + m_2)^{1/5}$ of two black holes with masses m_1 and m_2 in terms ofthe frequency of GW (f) and its time derivative ($\dot{f}$) is

$$M = \frac{(m_1 m_2)^{3/5}}{(m_1 + m_2)^{1/5}} = \frac{c^3}{G}\left[\frac{5}{98}\pi^{-8/3} f^{-11/3}\dot{f}\right]^{3/5}. \tag{31}$$

Using the waveform of GW150914, we obtain $M \approx 30 M_\odot$ and $m_1 + m_2 \leq 70 M_\odot$[16][17]. Taking the frequency and Schwarzschild radii of the binary components into consideartion,

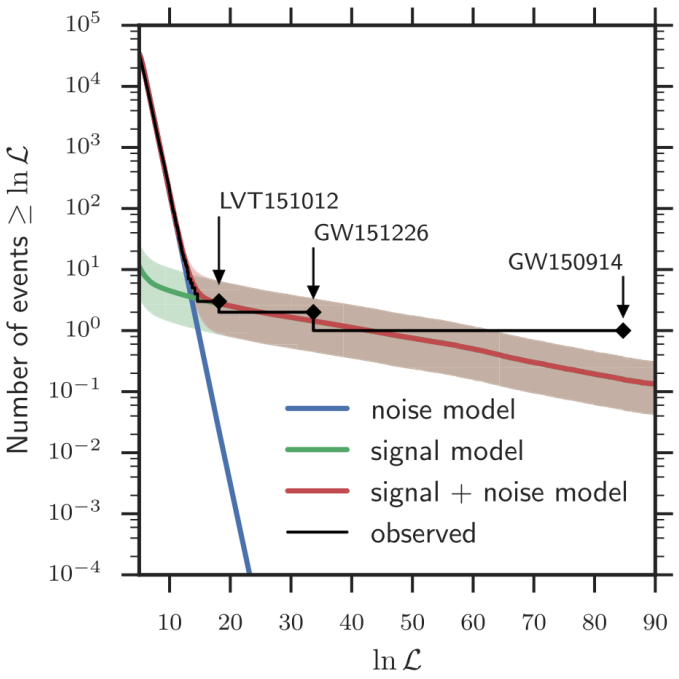

FIG. 7. The distribution of observed triggers as a function of the logarithm of likelihood $\mathcal{L}$.

BBH is the only choice so that they can orbit with each other without contacting at the orbital frequency of 75 Hz. More precisely, two independent methods (PyCBC and GstLAL) are used to search stellar-mass BBH signals. The parameter space spanned by mass $(m_{1,2},\ m_f)$, spin $(a_{1,2},\ a_f)$ is scanned by using a completed collection of template waveforms. The optimized fitting results of GW150914, GW151226 and LVT151012 are shown in figure 6. The dimensionless spin $a_{1,2}$ is defined as $a_{1,2} = c|S_{1,2}|/(Gm_{1,2}^2)$, where $S_{1,2}$ is the physical angular momentum.

The detection of GWs provides conclusive evidence of the existence of stellar-mass black holes. The least mass of these three BBHs is the secondary mass (m_z) of GW151226, which exceeds $5.2M_\odot$. Based on general relativity and the principle of causality, C. E. Rhoades and R. Ruffini showed that the maximum mass of a neutron star at hydrodynamic equilibrium cannot be larger than $3.2M_\odot$[18]. Above the critical mass, stellar-mass black holes are detected in X-ray binaries. Using 16 low-mass X-ray binaries, F. Ozel et al. inferred that the observation can be described as a narrow mass distribution at $7.8 \pm 1.2M_\odot$[19] and the number of black holes decrease rapidly at high-mass end. However, LIGO's three GW events push the frontier of stellar-mass black holes to $60 \sim 70M_\odot$ (GW150914 demonstrates that the total mass after merger is $m_{tot} \approx 65.3M_\odot$). Moreover, the high frequency of GW events shows that the population of stellar-mass blacks of $\sim 20M_\odot$ may be underestimated. Assuming a uniform distribution of BBH population in comoving frame, B. P. Abbott et al. calculated the rate of coalescing BBHs in local universe. The distribution of astrophysical and terrestrial triggers are illustrated in figure 7. At low likelihood, the distribution is dominated by noises while at high likelihood the astronomical signals are overwhelmingly favored. Hence, it is uncontested that GW150914 and GW151226 are indeed GW events and LVT151012 is more likely to be a signal instead of noise. The joint analysis of three events in LIGO's first run improves the BBH merger rate from $2 - 600\mathrm{Gpc}^{-3}\ \mathrm{yr}^{-1}$[20] to

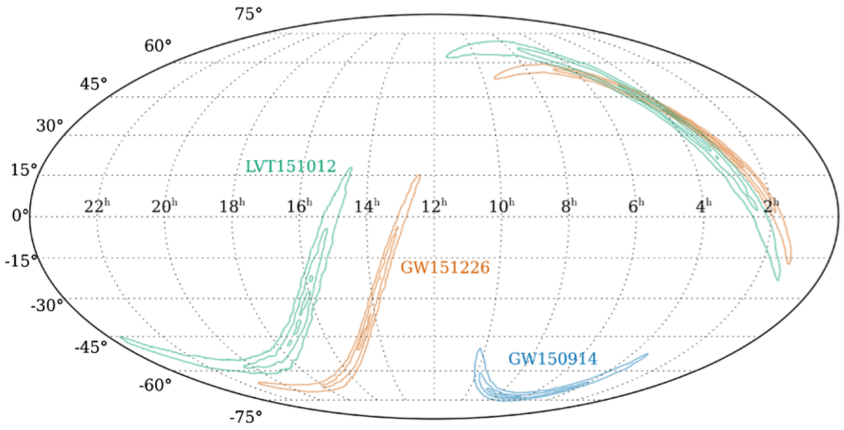

FIG. 8. The probability distributions of locations of GW150914, GW151226 and LVT151012 in equatorial coordinates.

$9-240\mathrm{Gpc}^{-3}\ \mathrm{yr}^{-1}$[15]. More GW events are expected to be detected in the future.

The distance dependence of strain h (equation 20) and energy flow S (equation 21) enables us to conclude the luminosity distance of GW sources. GW150914 and GW151226 have the similar distance of 420^{+150}_{-180}Mpc and 440^{+180}_{-190}Mpc[15], respectively. The signal of LVT151012 is quite dimmer and is inferred to locate at a larger distance $\sim 1000\pm500$Mpc. The conjecture of sky locations is based on the sequence and time difference between two detectors L1 and H1. The probability distributions of sky locations of GW150914, GW151226 and LVT151012 are shown in figure 8. Because only L1 and H1 detected these events, the locations are poorly constrained with the areas of 90% confidence are 230, 850 and 1600 deg^2, respectively.

After the LIGO team announced the detection of GW150914, *Fermi* group presented one alert of the Gamma-ray Burst Monitor (GBM) 0.4s after the GW event[21]. With a false alert probability of 0.0022 (2.9σ), the transient signal lasts $\sim$ 1s and does not show the feature of previously known source. Despite of the ill-constrained sky location, the direction of this transient signal is consistent with the location of GW150914. We cannot exclude the possibility that this transient signal comes from GW150914. Moreover, the IceCube Collaboration and ANTARES Collaboration searched the high-energy neutrino counterparts of GW150914 and no astrophysical neutrinos were detected by both detectors within the time interval $\pm$500s about the GW event. Based on the non-detection fact, the upper bound of total energy radiated in the form of neutrinos is estimated as $E_{\nu,tot} \approx 5.4\times10^{51}-1.3\times10^{54}$ erg[22]. With the constantly improved sensitivity of LIGO detectors and the source rate of $9-240\mathrm{Gpc}^{-3}\ \mathrm{yr}^{-1}$, we expect to detect more GW events and by then the astronomical sources and mechanisms can be better understood by using GWs and their X-ray/gamma-ray/neutrino counterparts.

III. ASTRONOMICAL SOURCES OF GRAVITATIONAL WAVES

Physics also solves puzzles. However, these puzzles are not posed by mankind, but rather by nature.
—Maria Goeppert-Mayer

The GWs we have seen are generated from dynamics that create a time-changing mass quadrupole moment. To produce a GW whose intensity is strong enough to be detected, we expect the source must have a large mass, a fast speed and a strong gravitational field. Usually, the frequency band of a GW is determined by the time scale of relevant dynamic processes. For instance, in a binary system, the frequency of GW is the double of the orbital frequency. We usually categorize the GW sources by the frequency band in which the GW is radiated. For example, gravitational waves with the frequency between ~ 1 Hz and ~ 1 kHz are classified to the high-frequency band; the band that is sensitive to ground-based laser interferometers, like LIGO and VIRGO. A list of potentially observable sources in different frequency band is given below,

1. GWs produced by the primordial stochastic background are classified to extremely low-frequency band with frequencies in the range $10^{-18} - 10^{-15}$ Hz. They can be sensed indirectly from the GW feature in the Cosmic Microwave Background.

2. Low-frequency (1 nHz - 1 Hz) GWs are usually generated in supermassive black hole binaries ($\sim 10^3 - 10^9 \mathrm{M}_\odot$) and can be detected by pulsar timing arrays and space-based laser interferometers like LISA.

3. Neutron star/black hole binaries with mass $1M_\odot \leq m \leq 10^3 M_\odot$, binary mergers, GRBs and supernovae are major contributors to GWs in high-frequency band (1 Hz - 1 kHz). As we can see in figure 3 (b), the high-frequency band is covered by LIGO's sensitive interval. Ground based laser interferometers and resonant antennas are capable of detecting GW signals in this frequency band.

This section will provide an overview consisting of physical processes, theoretical predictions and GW observations of these sources. To keep a coherent flow, we adapt the sequence listed in table I, from well-modeled transient waveforms (coalescing binary systems), GW burst (GRBs, supernovae and TDE) to continuous waveforms (e.g. stochastic GW backgrounds).

A. Coalescing binary systems

Among the potential sources of GWs, coalescing binary systems are the most promising candidates. At present, we are more confident to draw this conclusion since all GW events detected by LIGO are confirmed to be produced by the merger of BBHs. The binary systems usually refer to the systems that two compact stars, such as NS-NS, NS-BH and BH-BH, are orbiting around each other. Here NS and BH are abbreviations of neutron star and black hole, respectively. One common feature of these systems is that they can induce a strong time-varying quadrupole moments, which is required to produce strong GWs. Nevertheless, our model towards binary coalescence is incomplete. When the orbital velocity of components in a binary system approaches the speed of light, which is the occasion when merger occurs, the post-Newtonian approximation is invalid. In addition, for neutron stars,

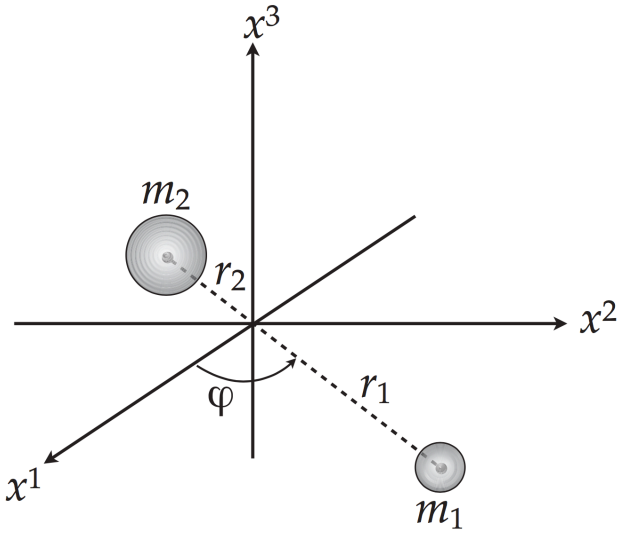

FIG. 9. Schematic diagram of a binary system orbiting in $x_1 - x_2$ $(x - y)$ plane. ϕ is the azimuth angle.

the tidal interaction would cause significant modifications to the waveform especially when the orbital radius is comparable to the radii of neutron stars. The high-speed rotating black holes may also provide unpredictable changes to the waveform through spin-spin or spin-orbital interactions. Considering all of these obstacles, it is a formidable task to find rigorous solutions. (The good news is that theoritists who work in the field do not need to worry about switching fields in the future once the model is so perfect that no further confinement is needed.)

Without attempting to strike the general problem, we will present the simplified model for waveforms in a coalescing binary system where only Kepler motion is considered. Despite of the simplification, quantitive conclusions of chirp mass, phase evolution and frequency dependence of $h_{\mu\nu}$ can provide some inspirations for future studies.

1. Radiation from orbiting binary systems

We start with the basic equations of GWs in section I.B.2 to derive the energy loss rate due to gravitational radiation and the frequency dependence of the strain, say $h = h(f)$. Consider a binary system consisting of two point masses m_1 and m_2. Without losing generality, we assume these two masses are orbiting around each other on the $x_1 - x_2$ plane and the orbital angular momentum points x_3 direction. Here, we ignore the spin for simplification. In the center-of-mass coordinates, positions of these two masses is represented by radius vectors $\boldsymbol{r}_1 = m_2\boldsymbol{r}/M$ and $\boldsymbol{r}_2 = -m_1\boldsymbol{r}/M$, where $\boldsymbol{r} = \boldsymbol{r}_1 - \boldsymbol{r}_2$ is the relative position vector and $M = m_1 + m_2$ is the total mass. The configuration is shown in figure 9. Using the definition of quadrupole moment $D_{\alpha\beta}$, we obtain the components:

$$D_{xx} = \mu r^2(3\cos^2\phi - 1),\ D_{yy} = \mu r^2(3\sin^2\phi - 1),\ D_{xy} = D_{yx} = 3\mu r^2\cos\phi\sin\phi, \qquad (32)$$

where $\mu = m_1 m_2/M$ is the reduced mass. For a stable binary system, the change of radius is negligible in one orbital period, $\frac{T|\dot{r}|}{r} \ll 1$. It is convenient to assume r is a constant to find the energy loss rate dE/dt and then calculate $\dot{r}$ to the first order using $E = -Gm_1m_2/(2r)$. Under this assumption and decompose $D_{\alpha\beta}$ to spherical unit vector $\hat{\theta}$ and $\hat{\phi}$, equation (22) gives

$$-\frac{dE}{dt} = \frac{32G\mu^2 r^4}{5c^5}\dot{\phi}^6 = \frac{32G^4 m_1^2 m_2^2 M}{5c^2 r^5}, \tag{33}$$

here the Kepler relation $\dot{\phi} = r^{-3/2}\sqrt{GM}$ is used. Now let us consider the long-term evolution of the orbit. Because the GW radiation takes away the kinetic energy, two masses are getting closer and closer. This effect is significant only in long-term evolutions and can be evaluated from dE/dt:

$$\dot{r} = -\frac{2r^2}{Gm_1m_2}\frac{dE}{dt} = -\frac{64G^3 m_1 m_2 M}{5c^5 r^3}. \tag{34}$$

It is crucial to realize that this equation is not valid for the merger of two compact objects when the orbital radius is close to the masse. Under such circumstance, the precondition $T|\dot{r}|/r \ll 1$ is violated.

In the late evolution stage of a binary system, energy and matter interactions become increasingly important. To understand the dynamics of a coalescing binary system, we need to find the frequency dependence of strain h, in other words, how the amplitude and frequency evolves with time. Combining $h_{ij} = -2G/(3c^4R)\ddot{D}_{ij}$ (derived from equation 20) and the quadrupole moment in equation (32), we obtain

$$\begin{aligned} h_+ &= -\frac{4G\mu r^2\dot{\phi}^2}{c^4 R}\cos 2\phi, \\ h_- &= -\frac{4G\mu r^2\dot{\phi}^2}{c^4 R}\sin 2\phi. \end{aligned} \tag{35}$$

Note that the frequency of GW is doubled comparing to the orbital frequency, $f_{GW} = 2f_{\text{orbit}} = \omega/\pi$. Rewriting the strain in terms of $v = r\dot{\phi}$ and introducing the angle of inclination i when the observer is not in the z axis, the GW waveform is

$$\begin{aligned} h_+ &= -\frac{2G\mu}{c^2 R}(1+\cos^2 i)\left(\frac{v}{c}\right)^2\cos 2\phi, \\ h_- &= -\frac{4G\mu}{c^2 R}\cos i\left(\frac{v}{c}\right)^2\sin 2\phi. \end{aligned} \tag{36}$$

It is obvious that the GW from one orbiting binary system is monochromatic when $\dot{\phi}$ does not change. Utilizing the energy loss rate in equation (33), we show that the evolution of waveform (characterized by f and $\dot{f}$) is determined uniquely by the chirp mass $\mathcal{M} = \mu^{3/5}M^{2/5} = (m_1m_2)^{3/5}(m_1+m_2)^{-1/5}$. According to the virial theorem, the total energy of a gravitational system is $E = -K/2$, where K is the total kinetic energy. we obtain $dE/dt = \mu c^2(v/c)(\dot{v}/c)$. Therefore, the equation (33) can be used to find the time-dependent of v:

$$\frac{d(v/c)}{dt} = \frac{32c^3\mu}{5GM^2}\left(\frac{v}{c}\right)^9. \tag{37}$$

Integrating equation (37) over v/c from zero to unity corresponds to the integration over

time from zero to t_c, the coalescence time. In terms of initial frequency, t_c is solved to be

$$t_c = \frac{5GM^2}{\mu c^3}\left(\frac{\pi GMf_0}{c^3}\right)^{-8/3}. \tag{38}$$

Since the GW frequency is $f = v^3/\pi GM$, the first-order time derivative of f is

$$\frac{df}{dt} = \frac{df}{dv}\frac{dv}{dt} = \frac{95}{5}\pi^{8/3}\left(\frac{G\mathcal{M}}{c^3}\right)^{5/3} f^{11/3}, \tag{39}$$

where $\mathcal{M}$ is previously defined as the chrip mass. Since $\frac{d\phi}{dv} = \frac{d\phi}{dt}\frac{dt}{dv}$ is in terms of v, the phase can be written as $\phi = \phi(f)$ considering the relation between v and f. Hence, f and $\dot{f}$ uniquely determine the waveform of GW. We thus can construct the waveform in terms of f or t. On the other hand, once the the waveform is reconstructed from GW signal, we can infer the chirp mass $\mathcal{M}$, coalescence time t_c and the angle of inclination i.

2. Predictions and Detectability

In 2010, J. Abadie et al. presented the coalescing rate of binary neutron stars based on the observed binary pulsars in our Galaxy[23]. For binary neutron star inspirals, the coalescence rate per Milky Way Equivalent Galaxy (MWEG) is estimated to be 100 Myr^{-1}. With the expected sensitivity of LIGO detectors, this merger rate corresponds to the binary neutron-star detection rate in the range 0.4 to 400 per year. For neutron star - black hole systems, the event rate is roughly 0.2 to 300 per year while a high detection rate of black hole - black hole system is obtained: 0.4 to 1000 per year. There are several ways to convert the galactic merger rate to a rate in the local universe. One is to assume that the binary system is determined by the star formation rate (SFR). By comparing the galactic SFR ($3M_\odot$ yr^{-1}[24]) with SFR of local universe $0.03M_\odot$ yr^{-1} Mpc^{-3}[25], we obtain the merger rate $\mathcal{R} \approx 400$ Gpc^{-3} yr^{-1}. Above all, we conclude that binaries are optimal GW sources. As discussed earlier, binary coalescences are usually divided into several phases where the dynamics and waveforms have distinct features. Here, we discuss these phases in details.

The binary inspiral is actuated by the energy loss processes. In this phase, binary orbits are assumed to be a slowly shrinking circular and frequency of GW is the twice of orbital frequency given by Kepler formula,

$$f_{GW} = \frac{1}{\pi}\left(\frac{G\mu}{r^3}\right)^{1/3} \approx 1.6\times10^{-3}\left(\frac{M}{1.4M_\odot}\right)^{1/2}\left(\frac{r}{10^{11}\mathrm{cm}}\right)^{-3/2}\ \mathrm{Hz}. \tag{40}$$

If the binary system consists of two white dwarfs with typical mass $1.4M_\odot$ and radius $r = 10^{11}$cm, the upper bound of GW frequency is $\sim 1.6\times10^{-3}$Hz. As for NS-NS, NS-BH, BH-BH binaries, the upper limit can be estimated using the Schwarzschild radius $r \sim 2R_s = 4GM/c^2$:

$$f_{GW,NS} \approx 10^3\left(\frac{3M_\odot}{M}\right)\mathrm{Hz}. \tag{41}$$

Based on this, we conclude that the normal frequency of these binaries is typically in the range $1 \sim 1000$ Hz. In time domain, the amplitude of strain in equation (36) can be

expressed in terms of f using $f = \frac{v^3}{\pi GM}$:

$$h^T \sim \frac{G\mu}{c^2 R}\frac{v^2}{c^2} = \frac{\mu}{c^4 R}\left(\frac{Gf^2}{\pi M^2}\right)^{1/3}. \tag{42}$$

Instead of the strain in time domain, the characteristic amplitude detected by GW detectors is the amplitude of corresponding Fourier series, $h^F(f) \sim \sqrt{N}h^T(f)$[26], where $N = f^2(df/dt)^{-1}$ is the number of circles that the binary undergoes while the frequency of the wave changes an amount of f. Combining the expression of df/dt in equation (39) we obtain the frequency dependence of h^F

$$h^F(f) \propto f^{-1/6}. \tag{43}$$

This relation will later be used to discuss the detectability of the inspiral phase.

At the end of inspiral phase, the binary companions will contact and rapidly plunge together. In this process, the formulism we previously constructed in this paper is no longer valid and numerical simulations are required. E. Flanagan and E. Hughes (1998) and S. Kobayashi and P. Meszaros (2003) showed that the frequency band of the deformed core/disk in this phase is narrow[26][27]. To the simplest form, the deformation can be considered as a bar. The mean strain is given by

$$h^F \approx 1.9 \times 10^{-21}\left(\frac{R}{10\text{Mpc}}\right)^{-1}\left(\frac{r}{10^6\text{cm}}\right)^{-1}\frac{m_1 m_2}{M_\odot^2}. \tag{44}$$

Later in this evolution, GWs are produced from the rqpid vibrations of the ellipsoid, this stage is named as ring-down of binary coalescence. In this phase, the frequency reaches the upper bound

$$f_q(a) \approx 32F(a)\left(\frac{M}{M_\odot}\right)^{-1}\ \text{kHz}, \tag{45}$$

where $F(a) = 1 - 0.63(1-a)^{3/10}$ and a is dimensionless spin parameter of the new-forming black hole. The characteristic GW amplitude at f_q is given by

$$h^F \sim 2.0 \times 10^{-21}\left(\frac{R}{10\text{Mpc}}\right)^{-1}\ \frac{\mu}{M_\odot}, \tag{46}$$

here, $Q(a) = 2(1-a)^{-9/20}$. Derivation of equation (44)-(46) is out of scope of this paper and can be found in [28].

One application of equations disused in this section if to calculate the GWs produced by GRB progenitors. Potential progenitors of normal GRBs can be classified into two categories, binary mergers (such as double neutron stars, black hole - neutron stars and black hole - while dwarf) and fast-rotating massive stellar collapses. S. Kobayashi and P. Meszaros (2003) showed their results of GWs produced in the first scenario. Figure 10 illustrates the comparison between LIGO sensitivity $\sqrt{[fS(f)]}$ and GW signals from double neutron stars (DNS) and neutron star - black hole (NSBH). They also discussed the detectability of black hole - while dwarf and black hole - helium star scenarios and found that these two kinds of progenitors are not likely to be detected by LIGO, due to the relatively weaker strains.

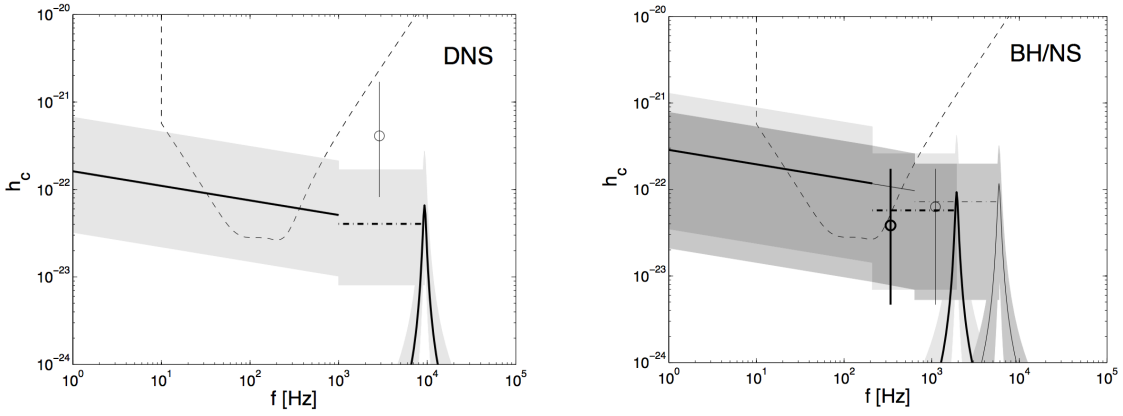

FIG. 10. GWs intensitis from double neutron stars (left panel) and neutron star-black hole (right panel) compared to the LIGO sensitivity (dashed line). In both figures, solid line, dot-dashed line and solid spike correspond to inspiral, merger and ring-down phases, respectively

B. Gravitational collapse

We now consider gravitational radiation from the collapses of massive stars. There are several collapsing channels depending on the mass of progenitors and the environment. When the fusion fuels in a lightly massive star ($\leq 8M_\odot$) get exhausted, a white dwarf, in which gravity is balanced by electron degeneracy pressure will be produced as a remnant. If a white dwarf is in a binary system and gains mass from its companion, accretion-induced collapse may occur once the mass of the while dwarf exceeds Chandrasekhar mass limit ($\sim 1.4M_\odot$). During the collapse, if the nuclear reactions are ignited due to the high temperature and pressure, the white dwarf will explode and a Type Ia supernova is produced. Typically, stars with mass larger than $8M_\odot$ will end their lives through core collapse and a neutron star or a black hole rather than white dwarf will be produced. In this scenario, the collapse triggers Type II supernovae as well as Type Ib/c supernovae. As is mentioned in the last section, some long-duration GRBs are believed to be formed by more violent collapses when black holes are produced. Very massive stellar-mass stars ($\geq 50M_\odot$) are capable of collapsing into black holes without undergoing supernovae. Despite these scenarios has been established for decades, we still cannot fully understand the parameters and processes related to the stellar evolution. Nevertheless, with the development of GW astronomy, we gained one powerful tool to depict the physical picture of stars especially the relevant non-spherical dynamics.

The conservation of angular momentum predicts that the white dwarfs, neutron stars and black holes formed from collapses are usually fast-spinning, which also demonstrats that these products are promising GW radiators. If the new born proto-star is rapidly spinning, its shape can be extremely deformed from a sphere to a bar, due to the intense centrifugal force. This still occurs even the collapse is spherically symmetrical. In this section, we will calculate the GW strains from the collapse phase and the bar phase.

1. Modeling the GWs from collapses

Let us consider an axisymmetric collapse of a stellar core rotating with the angular momentum L. According to the conservation of angular momentum, the matter near the

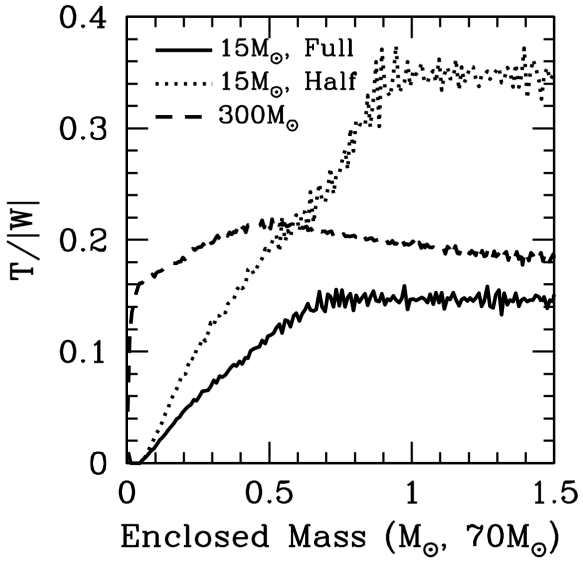

FIG. 11. Rotational energy divided by the gravitational energy $\beta = E_{rot}/E_G$ versus mass of collapse.For dotted and solid lines, the x axis is in the unit of $70M_\odot$ while the dashed line represent a 300 $M_\odot$ scale.

axis falls inward faster than the matter near the equator. Hence, the spherical core becomes an axisymmetric ellipsoid. The eccentricity is $e \approx L/\sqrt{GM^3 r}$, where M is the mass of the core and r is the equatorial radius. As we can see, the eccentricity increases as the size decreases. Before the density of the core reaches the nuclear density, the duration collapse is estimated as the free-fall timescale

$$t_{dyc} \approx t_{ff} = \left(\frac{3\pi}{32G\rho}\right)^{1/2} \sim 0.1\text{ms}. \tag{47}$$

Here, we assume the density of final stage of the collapse is the nuclear density 10^{18}kg m^{-3}. For a biaxial ellipsoid with a uniform density distribution and the axis pointing z direction, the principle moments of inertia are $D_{xx} = D_{yy} = \frac{2}{5}Mr^2(1 - e^2/2)$ and $D_{zz} = \frac{2}{5}Mr^2$. There is no GW along z axis while observers on the equatorial plane will detect the strongest strain, which is given by

$$h \approx \frac{G}{c^4}\frac{\ddot{D}_{xx} - \ddot{D}_{zz}}{R} \sim \frac{GM}{c^2 R}\left(\frac{er}{ct_{dyc}}\right)^2 \sim 10^{-20}\left(\frac{R}{10\text{kpc}}\right)^{-1}\left(\frac{M}{1M_\odot}\right) \tag{48}$$

with $e \sim 0.1$. Note that the radius 10kpc is the characteristic distances of supernovae in the Galaxy.

When the core is rapidly rotating, GWs can be radiated from the non-axisymmetric motion. In such situation, the geometry of stellar core can be simplified as a bar with a rapidly varying quadrupole moment. Bar-mode instability is stimulated when centrifugal potential energy E_{cen} becomes significant comparing to the gravitational potential energy E_G. If the ratio $\beta = E_{cen}/|E_G|$ is significant, the object is unstable on a secular time scale[29]. Dynamic instability occurs when $\beta \geq 0.27$. According to modern progenitor models, the

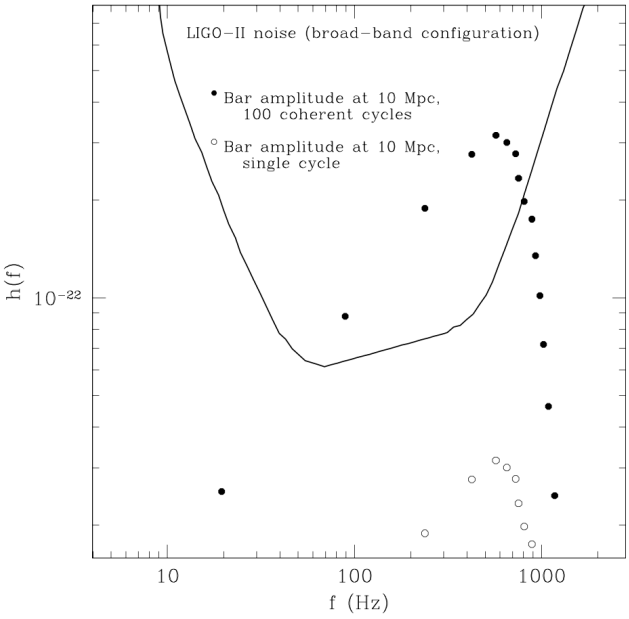

FIG. 12. Strains of bar-mode GWs.

rotation speed of collapse is relatively lower comparing to early models. However, the rotational energy can be comparable to the gravitational potential energy (see figure 11). Using equation (20), we obtain the root-mean-square gravitational strain for a bar of mass m, length $2l$ and angular velocity ω:

$$h = \sqrt{\frac{32}{45}} \frac{Gmr^2\omega^2}{c^4 R}. \tag{49}$$

Analogous to binaries, the frequency of GW emissions is twice the rotational frequency. In the bar mode, the clumps of collapsing material can rotate around the core with collapse processes. This will induce fragmentation instability as indicated from some simulations [30]. GWs generated from this instability can be classified to binary systems and we can use equation (36) to estimate the corresponding gravitational strains.

2. Results of GW emission

Using equations we obtained in previous section, we can now calculate the gravitational strains for two important cases - supernovae and GRB progenitors. For each scenario, we summarize the expected gravitational strains from bar instabilities.

The supernovae rate is well constrained in an interval between 1 per 50-140 years per galaxy. However, we also need to consider the distribution of angular velocity or angular momentum to determine the applicability of bar model. According to Chernoff & Cordes, the initial spin periods of pulsars can be fitted using a Gaussian function with the average $\bar{P} = 7$ms and sub-ms pulsars lying behind the 2σ tail. Based on the bar model, C. Fryer et al (2002) showed the strains of core-collapse supernovae (see figure 12). In their calculation, they assume all mass inside a radius will participate the bar instability. In figure 12, from

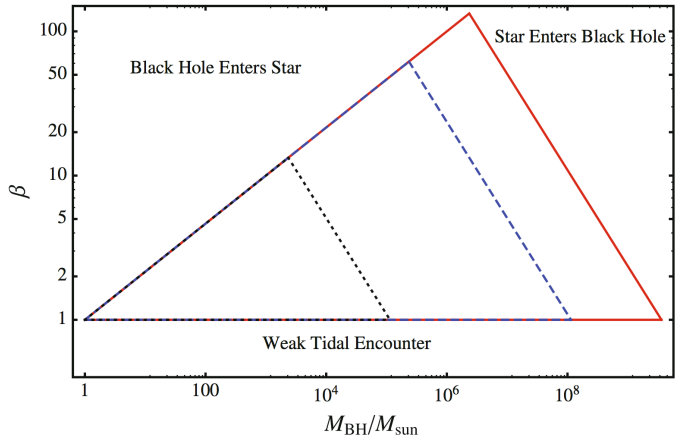

FIG. 13. The parameter space of tidal disruption events. A star with the corresponding β lying in its respective trangel can be disrupted by the black hole.

left to right, the dots represent strains from a increasing sequence of radii. The closed dots are obtained by assuming the bar mode exists in 100 GW periods while the open dots correspond to the signal circle duration. As we can see from figure 12, At 10 Mpc, the collapses with short-duration bar mode are potentially to be detected by LIGO. In 2013, A. Corsi and P. Meszaros[31] investigated the connection between X-ray afterglow of GRBs and the formation of millisecond magnetars. In this scenario, they found that the GWs from the bar instability of nascent neutron star can be detected un to a distance of 100 Mpc. The GW signals are typically accompanied with an afterglow light curve plateau from GRBs, which demonstrates that the joint searches for collapsars as GRB progenitors are possible.

C. Tidal disruption events

It has long been believed that most galaxies harbor one or more supermassive black holes (SMBHs) with masses in the range $10^5 - 10^9 M_\odot$. A tidal disruption event occurs when a star gets sufficiently close to a SMBH and is pulled into debris by the strong tidal force. Because TDE typically occurs with flares of electromagnetic radiation and GW emissions, TDEs provide an important method to probe SMBHs in active galaxies.

In the Newtonian picture, for a star of M and radius R orbits around a black hole of mass M_{BH}, the critical orbital radius of tidal disruption is [32]

$$R_T = R\left(\frac{M_{BH}}{M}\right)^{1/3} \approx 10^{12}\left(\frac{M_{BH}}{10^6 M_\odot}\right)^{1/3}\left(\frac{M}{M_\odot}\right)^{-1/3}\frac{R}{r_\odot}\ \text{cm} \tag{50}$$

Most astrophysical TDEs are expected to be formed from zero-energy, parabolic orbits. If the minimum pericenter distance R_P satisfies $R_P \leq R_T$, the self gravitational binding force cannot resist the tidal force and the star will be disrupted. The strength of disruption events can be measured by a dimensionless parameter $\beta = R_T/R_P$. On the other hand, for a SMBH, the horizon radius increases linearly with M_{BH}, i.e. $R_s = 2GM_{BH}/c^2$, there exists

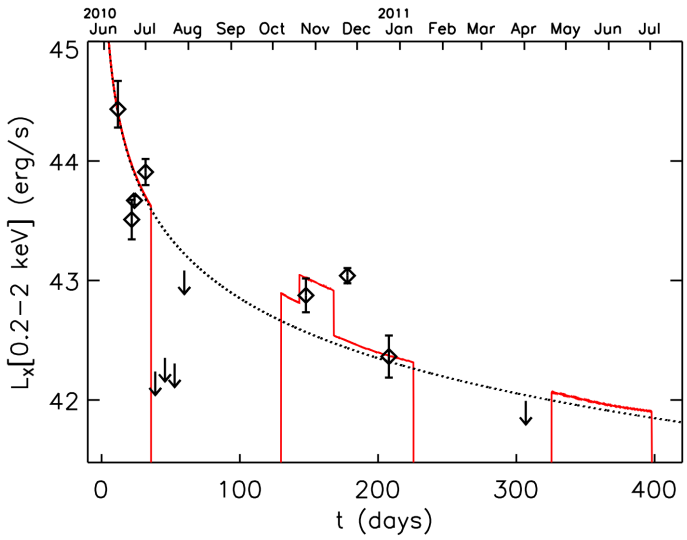

FIG. 14. Light curve of X-ray flare from SDSSJ120136.02+300305.5, based on XMM-Newton and Swift observations. Red solid line is the prediction given by[34].

a critical mass (Hill mass) of the SMBH that is derived from $R_s = R_T$,

$$M_{Hill} = 1.1 \times 10^8 M_\odot \left(\frac{R}{R_\odot}\right)^{3/2} \left(\frac{M}{M_\odot}\right)^{-1/2}, \tag{51}$$

above which stars will be absorbed to the black hole prior to tidal disruption. In this case, electromagnetic signals are uninteresting despite GW signals are still radiated. Taking the constraints of β and M_{BH} in to consideration, the parameter space of TDEs is illustrated in figure 13[33]. The three triangles are calculated for solar-type stars (blue dashed), red giants with $M = M_\odot$, $R = 10R_\odot$ (red solid) and white dwarf with $M = M_\odot$ and $R = 0.01R_\odot$ (black dotted). If $\beta < 1$, no TDE occurs. The left upper sides of thees trangles represent $R = R_P$. If $R > R_P$, the black hole will be swallowed by the star while the right upper sides correspond to the condition $R_P < R_T = R_s$.

TDEs can produce detectable flares extending from gamma-ray to radio bands. A comprehensive review of the status of observations can be found in [35] and references therein. Here, we high light one TDE observed by $Swift$ and $XMM - Newton$. Among the TDEs in XMM-Newton's X-ray survey, SDSSJ120136.02+300305.5 has the the best recorded first-year light curve due to the follow-ups with XMM-Newton and Swift, as shown in figure 14. From this figure we find that the peak luminosities are up to $\sim 10^{44}$erg s^{-1} in the soft X-ray band. The time scale of X-ray lightcurve decay is several months. Besides, the data points are consistent with the power law $L \propto t^{-5/3}$, as predicted by the disruption theory [36].

Besides the electromagnetic emissions, TDEs also generate GWs that are detectable to LISA. In [37], S. Kobayashi et al. showed that the GW strain from tidal disruptions is approximately

$$h \sim \frac{GMR_s}{c^2 r R_P} \approx 2 \times 10^{-22} \beta \left(\frac{r}{10\text{Mpc}}\right)^{-1} \left(\frac{R}{1R_\odot}\right)^{-1} \left(\frac{M}{M_\odot}\right)^{4/3} \left(\frac{M_{BH}}{10^6 M_\odot}\right)^{2/3} \tag{52}$$

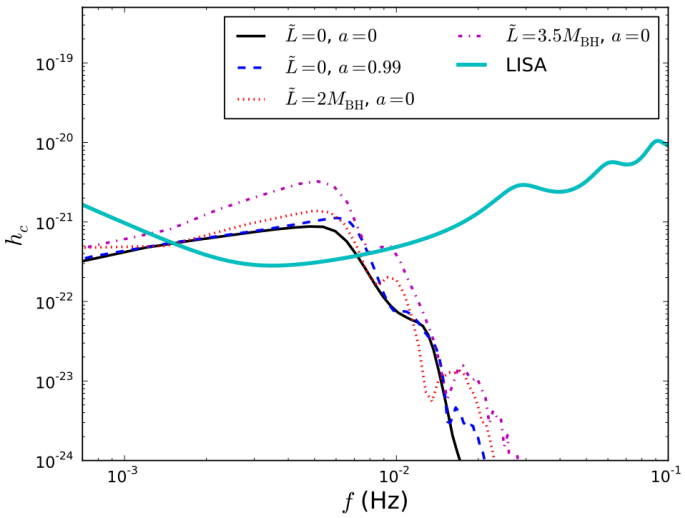

FIG. 15. Characteristic GW strains with $M = 2M_\odot$ and $M_{BH} = 10^6 M_\odot$. The LISA noise curve is also shown in the figure.

at the frequency

$$f \sim \sqrt{\frac{GM_{BH}}{R_P^3}} \approx 6 \times 10^{-4}\text{Hz}\ \beta^{3/2} \left(\frac{M}{M_\odot}\right)^{1/2} \left(\frac{R}{R_\odot}\right)^{-3/2}. \tag{53}$$

Employing a three-dimensional relativistic smoothed particle hydrodynamics (SPH) code, they presented GW waveforms and strains from the disruptions of solar-type stars (figures 4 - 7 in [27]) and Helium stars (figure 8). In both cases, the GW bursts can be detectable to LISA up to the distance $r \approx 20$Mpc. W. East (2014) considered the modification to GW strains due to black hole spins and found that collisions with angular momentum can substantially boost the GW strength[38]. The characteristic GW strains from main-sequence star disruptions are shown in figure 15. In the figure, angular momentum $L = GM/c^3$ are written in geometric units with $G = c = 1$. Moreover, the TDE rate is estimated in the range $10^{-5} - 10^{-3}\text{yr}^{-1}$ per galaxy, which demonstrates that TDEs are likely to be detected by space-based interferometers.

D. Stochastic GW backgrounds

Other than the GW individual sources discussed in previous sections, there exists a gravitational-wave background distributed over the sky. At cosmological distance, GWs from these individual sources can overlap with each other and it becomes impossible to differentiate the respective contributors from the superposition of their GW signals. In this case, the GW spectra of individual sources become less important. Nevertheless, the background encodes information of cosmological evolutions and stellar distributions. Since the sum of signals obeys Gaussian distribution, guaranteed by the central limit theorem, the GW background is named as stochastic background. Despite that we no longer need to

analyze the GW spectra source by source, the random nature of stochastic GW backgrounds makes it challenging to distinguish the signals from noises. One solution to this problem is using two detector with uncorrelated noise function to extract the signals, as implemented by LIGO. In this section, we will focus on cosmological as well as astronomical sources of stochastic backgrounds of gravitational waves.

Analogous to the cosmic microwave background (CMB), the afterglow of radiation from early universe, GWs are generated within a short time after the Big Bang. Comparing to electromagnetic field of CMB, gravitational interactions have a much smaller coupling constant which results in a much shorter decoupling time, the Planck time $t_P = \sqrt{\hbar G/c^5} \approx 10^{-43}s$[39] after the Big Bang. Unfortunately, GWs from Planck era are not detectable due to the inflation of early universe. If inflation indeed happened, the wavelength of GWs from cosmic sources at that time is comparable to the size of universe (i.e. the Hubble length c/H) which can be evaluated from current value $l_0 = c/H_0 \approx 10^{26}$ m. Assuming a flat Friedmann-Lemaitre-Robertson-Walker cosmology (or FLRW cosmology), the Hubble length is proportional to time and $\lambda_1 = (t_1/t_0)l_0$, where λ_1 is the wavelength of cosmic gravitational-wave background (CGWB) at cosmos time t_1 and t_0 is current time. Note that in the radiation-dominant universe, the redshift of wavelength is scaled as $\sqrt{t}$ while in the matter-dominant universe the redshift scales wavelength as $t^{2/3}$. Hence, considering the redshift evolution of λ due to cosmological expansion, the current GW wavelength is

$$\lambda_0 = \frac{t_1^{1/2}}{t_0^{1/3} t_{eq}^{1/6}} l_0, \tag{54}$$

where t_{eq} is the time when matter density is equal to radiation density. Take $t_1 = 10^{-35}$s when the universe is described by Grand Unified Theory (GUT), we obtain the wavelength at current time $\lambda_{GUT}(t_0) = 300$ m, corresponding to the frequency 10^8 Hz. This frequency is far more larger than the sensitive bands of current GW detectors. On the other hand, from equation (54), we conclude that the gravitational-wave background generated 10^{-23}s after the Big Bang is visible to LIGO (at the most sensitive frequency ~ 100 Hz) while 10^{-15}s for LISA at $\sim$0.01 Hz. Thus, cosmological GW backgrounds provide us an early glimpse of the Universe.

Now, we concentrate on the energy density spectrum of stochastic background. As in [40], we define the density parameter of GW background

$$\Omega_{GW} = \frac{1}{\rho_c} \frac{d\rho_{GW}}{d \ln f}, \tag{55}$$

where $\rho_c = cH^2/(8\pi G)$ is the critical density. B. Allen (1996) showed the relationship between gravitational-wave power spectral density $S_h(f)$ and $\Omega_{GW}(f)$:

$$S_h(f) = \frac{3H_0^2}{2\pi} \frac{\Omega_{GW}(f)}{f^3}. \tag{56}$$

As for detectors, e.g. LIGO and VIRGO, the characteristic strain spectrum is defined as $h_c(f) = \sqrt{f S_h(f)}$. Hence, in terms of $h_c(f)$, the density parameter of GW background is

$$\Omega_{GW}(f) = \frac{2\pi^2}{3H_0^2} f^2 h_c^2(f). \tag{57}$$

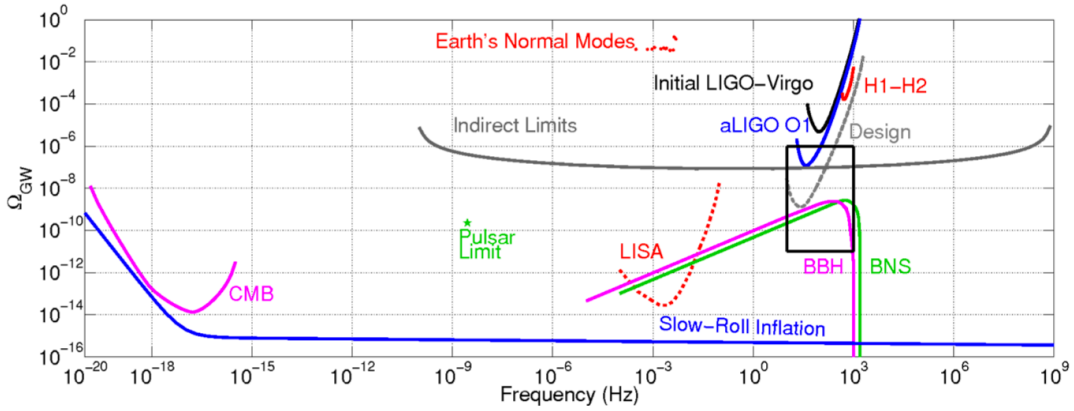

FIG. 16. Constraints on stochastic GW backgrounds ($\Omega_{GW}(f)$ v.s. f). Meanings of these lines are given in the text.

Usually, one detector only cover one small frequency band of the GW background, thus it is reasonable to confine our attention to a power-law spectrum, i.e. $\Omega_{GW,\alpha} = \Omega_\alpha (f/f_{ref})^\alpha$, where α indicates the spectral index and f_{ref} is a reference frequency. This definition naturally follows that $h_c(f)$ is also a power-law function with the index $\alpha = 2\beta + 2$, i.e. $h_c(f) = h_{c,\beta}(f/f_{ref})^\beta$ and $\Omega_{2\alpha+2} = 2\pi^2 h_{c,\alpha}/(3H_0^2)$. For GW background from inflationary cosmology, we usually assume a constant spectrum with $\alpha = 0$ and $\Omega_{GW,0} = \Omega_0$. For a background generated by coalescing binaries $\Omega_{GW,2/3}(f) = \Omega_{2/3}(f/f_{ref})^{2/3}$ [41].

The data from LIGO's first observing run shows no evidence of stochastic gravitational-wave signals. Based on that, B. Abbott et al (2017) reported the latest constraints on Ω_0 and $\Omega_{2/3}$ by employing the cross-correlation method for the pair LIGO detectors[42]. Comparing with the previous obtained from 2009-2010 LIGO and Virgo Data [43], the upper limits of Ω_0 and $\Omega_{2/3}$ in the frequency interval $20-85.8$ Hz are improved to 1.7×10^{-7} and 1.3×10^{-7}[44] at 95% confidence, respectively. To model the background contributed by coalescing binaries, they divided the population of compact binaries into categories labelled by k and the parameters, such as masses, of each group are labelled by θ_k. The overall contribution to the background is then

$$\Omega_{GW}(f) = \frac{f}{cH_0}\sum_k \int dz \frac{R_m(z;\theta_k)}{(1+z)E(\Omega_M,\Omega_\Lambda,z)}\frac{dE_{GW}}{df}(f_s;\theta_k) \tag{58}$$

where $R_m(z;\theta_k)$ is the binary merger rate (of k-kind binaries) per unit co-moving volume per unit time, dE_{GW}/df is the energy spectrum emitted by on single binary evaluated in the frequency $f_s = (1+z)f$ and $E(\Omega_M,\Omega_\Lambda,z) = \sqrt{\Omega_M(1+z)^3+\Omega_\Lambda}$ represent the cosmological effect on the distance. Details pertaining the selection of each function and parameter can be found in [44] and references therein. The expected contributions to $\Omega_{GW}(f)$ from binary black holes and binary neutron stars is shown in figure 16 (as labelled by BBH and BNS, respectively). This figure also shows the constraints from GWs by LIGO's first observing run (aLIGO O1), initial LIGO-VIRGO data and CMB. The line labelled by $Slow-RollInflation$ represents the background contributed by slow-roll inflation with a tensor-to-scalar-ratio $r = 0.11$[45]. Besides, the expected sensitive curve of LISA is also shown as the dashed red line. From this figure, we find the GW backgrounds from coalescing binaries (BBH and

BNS) cross with LISA's sensitive curve, which demonstrates that the corresponding GW signals may be detectable by LISA.

IV. REMARKS

Somewhere, something incredible is waiting to be known.
— Carl Sagan

Gravitational waves are one of the most inspiring predictions of general relativity, and provide an unprecedented probe of extreme gravity environments in the Universe. The first direct detection of GW has a particular meaning to both fundamental physics and astronomy.

As one of the foundations of modern physics. general relativity is well tested by the perihelion advance of Mercury and gravitational lensing effect. These observations provided strong implications that general relativity is correct. Gravitational wave, which is precisely predicted by the field equation, also agrees perfectly with the observations as expected. Moreover, GWs were in return been used to test the principle of equivalence to an unprecedented precision[46][47]. However, we still need to face the fact that the general relativity is not completed. It has been proved in 1970s that the space-times may become singular under some circumstances[48]. One example is the Big Bang which is believed to be the origin of the Universe. Essentially, singularity indicates that the theory is applied to the conditions that are beyond the realm of applicability. In this case, appropriate modifications or a substitutive theory is required to eliminate the divergence. As discussed previously, cosmological GWs generated in the early universe have the potential to be detected by current devices. In the future, GWs may become a powerful tool to study and test the physics of very early universe.

As for astronomy and astrophysics, using GWs, we stand to learn a great deal about astronomical phenomena that are inaccessible to electromagnetic telescopes. Since GWs reveal how a mass is changed and interact faintly with the ambient medium, we can use it to study the dynamics of opaque sources which is dim to electromagnetic telescopes due to the optical absorption. Hence, with the participation of GWs, we can see more things that are once impossible for optical telescopes. Furthermore, for the previously observed objects, GWs can be used to study the physical mechanisms from a brand new point of view. One puzzle in astronomy is the population of stellar-mass black holes in local universe. Previous evidence majorly relies on the observation of X-ray binaries. Now, the whole picture of the evolution of binary systems, including the orbital circulation, inspiral, merger and ringdown, can be depicted precisely using GWs. For example, from the GW waveform, we can directly calculate the chirp mass and further conclude the mass ratio through relativistic simulations. In addition, cross validations from multi-messenger method may improve the constraints of parameters to an unprecedented level of accuracy. Once the LISA is launched or the successors of LIGO come in to operate, there will be increasing implications to physics and astronomy.

ACKNOWLEDGMENTS

The author would like to thank Professor Peter Mészáros for his guidance through the whole semester. This article would not have seen the light of day without him. Thanks also to Professor B.S. Sathyaprakash, several sections in this article were inspired by his

presentation in a gravitational-wave colloquium.

---

[1] *Nobel Prize in Physics 1936: Presentation Speech* (1936-12-10).

[2] B. P. Abbott *et al.*, Phys. Rev. Lett. **116**, 061102 (2016).

[3] S. Weinberg, *Gravitation and Cosmology: Principles and Applications of the General Theory of Relativity* (2013).

[4] L. Landau and E. Lifshitz, *The Classical Theory of Fields* (1987).

[5] J. Creighton and W. Anderson, *Gravitational-Wave Physics and Astronomy* (2011).

[6] J. Weber, Phys. Rev. Lett. **117**, 206 (1960).

[7] J. Weber, Phys. Rev. Lett. **18**, 498 (1967).

[8] J. Weber, Phys. Rev. Lett. **20**, 1307 (1968).

[9] J. Weber, Phys. Rev. Lett. **17**, 1228 (1966).

[10] J. Aasi *et al.*, Classical and Quantum Gravity **32**, 074001 (2015).

[11] G. M. Harry and the LIGO Scientific Collaboration, Classical and Quantum Gravity **27**, 084006 (2010).

[12] B. Abbott *et al.*, Nuclear Instruments and Methods in Physics Research Section A: Accelerators, Spectrometers, Detectors and Associated Equipment **517**, 154 (2004).

[13] B. Abbott *et al.*, Classical and Quantum Gravity **32**, 074001 (2015).

[14] B. P. Abbott *et al.* (LIGO Scientific Collaboration and Virgo Collaboration), Phys. Rev. Lett. **116**, 241103 (2016).

[15] B. P. Abbott *et al.* (LIGO Scientific Collaboration and Virgo Collaboration), Phys. Rev. X **6**, 041015 (2016).

[16] B. P. Abbott *et al.* (LIGO Scientific Collaboration and Virgo Collaboration), Phys. Rev. Lett. **116**, 241102 (2016).

[17] B. P. Abbott *et al.* (LIGO Scientific Collaboration and Virgo Collaboration), Phys. Rev. D **93**, 122003 (2016).

[18] C. E. Rhoades Jr and R. Ruffini, Physical Review Letters **32**, 324 (1974).

[19] F. Özel, D. Psaltis, R. Narayan, and J. E. McClintock, The Astrophysical Journal **725**, 1918 (2010).

[20] B. P. Abbott *et al.*, The Astrophysical Journal Letters **833**, L1 (2016).

[21] V. Connaughton *et al.*, The Astrophysical Journal Letters **826**, L6 (2016).

[22] A. Albert *et al.* (ANTARES Collaboration and IceCube Collaboration and LIGO Scientific Collaboration and Virgo Collaboration and others), arXiv preprint arXiv:1703.06298 (2017).

[23] J. Abadie, B. Abbott, R. Abbott, M. Abernathy, T. Accadia, F. Acernese, C. Adams, R. Adhikari, P. Ajith, B. Allen, *et al.*, Classical and Quantum Gravity **27**, 173001 (2010).

[24] Y. Gao and P. M. Solomon, The Astrophysical Journal **606**, 271 (2004).

[25] J. Gallego, J. Zamorano, A. Aragon-Salamanca, and M. Rego, The Astrophysical Journal Letters **455**, L1 (1995).

[26] E. E. Flanagan and S. A. Hughes, Physical Review D **57**, 4535 (1998).

[27] S. Kobayashi and P. Mészáros, The Astrophysical Journal **589**, 861 (2003).

[28] F. Echeverria, Physical Review D **40**, 3194 (1989).

[29] S. Chandrasekhar, *Ellipsoidal figures of equilibrium*, Vol. 9 (Yale University Press New Haven, 1969).

[30] C. L. Fryer, D. E. Holz, S. A. Hughes, and M. S. Warren, in *Stellar Collapse* (Springer, 2004)

pp. 373–402.
[31] A. Corsi and P. Mészáros, The Astrophysical Journal **702**, 1171 (2009).
[32] J. Hills, The Astrophysical Journal **235**, 986 (1980).
[33] J.-P. Luminet and B. Pichon, Astronomy and Astrophysics **209**, 103 (1989).
[34] F. Liu, S. Li, and S. Komossa, The Astrophysical Journal **786**, 103 (2014).
[35] S. Komossa, Journal of High Energy Astrophysics **7**, 148 (2015).
[36] E. Phinney, in *Symposium-International Astronomical Union*, Vol. 136 (Cambridge University Press, 1989) pp. 543–553.
[37] S. Kobayashi, P. Laguna, E. S. Phinney, M. Peter, *et al.*, The Astrophysical Journal **615**, 855 (2004).
[38] W. E. East, The Astrophysical Journal **795**, 135 (2014).
[39] A. Vilenkin, Physics Letters B **117**, 25 (1982).
[40] B. Allen, in *Relativistic Gravitation and Gravitational Radiation, Proceedings of the Les Houches School of Physics, held in Les Houches, Haute Savoie*, Vol. 26 (1997) pp. 373–418.
[41] E. Thrane and J. D. Romano, Physical Review D **88**, 124032 (2013).
[42] B. Allen and J. D. Romano, Physical Review D **59**, 102001 (1999).
[43] J. Aasi *et al.*, Physical review letters **113**, 231101 (2014).
[44] B. o. Abbott, Physical Review Letters **118**, 121101 (2017).
[45] P. Ade *et al.*, Astronomy & Astrophysics **594**, A13 (2016).
[46] X.-F. Wu, H. Gao, J.-J. Wei, P. Mészáros, B. Zhang, Z.-G. Dai, S.-N. Zhang, and Z.-H. Zhu, Physical Review D **94**, 024061 (2016).
[47] E. Barausse, arXiv preprint arXiv:1703.05699 (2017).
[48] R. Penrose, in *General relativity* (1979).